nature electronics

Article

https://doi.org/10.1038/s41928-023-01075-y

Clean assembly of van der Waals heterostructures using silicon nitride membranes

Received: 20 January 2023

Accepted: 31 October 2023

Published online: 5 December 2023

Check for updates

Wendong Wang[1,2,9], Nicholas Clark[2,3,9] ✉, Matthew Hamer[1,2,9], Amy Carl[1,2,9], Endre Tovari[1,2], Sam Sullivan-Allsop[2,3], Evan Tillotson[2,3], Yunze Gao[1,2], Hugo de Latour[2,3], Francisco Selles[1,2], James Howarth[1,2], Eli G. Castanon[1,2], Mingwei Zhou[1,2], Haoyu Bai[4], Xiao Li[1,2], Astrid Weston[1,2], Kenji Watanabe[5], Takashi Taniguchi[5], Cecilia Mattevi[4], Thomas H. Bointon[2], Paul V. Wiper[6], Andrew J. Strudwick[6], Leonid A. Ponomarenko[1,7], Andrey V. Kretinin[1,2,3], Sarah J. Haigh[2,3], Alex Summerfield[2] ✉ & Roman Gorbachev[1,2,8] ✉

Van der Waals heterostructures are fabricated by layer-by-layer assembly of individual two-dimensional materials and can be used to create a wide range of electronic devices. However, current assembly techniques typically use polymeric supports, which limit the cleanliness—and thus the electronic performance—of such devices. Here, we report a polymer-free technique for assembling van der Waals heterostructures using flexible silicon nitride membranes. Eliminating the polymeric supports allows the heterostructures to be fabricated in harsher environmental conditions (incompatible with a polymer) such as at temperatures of up to 600 °C, in organic solvents and in ultra-high vacuum. The resulting heterostructures have high-quality interfaces without interlayer contamination and exhibit strong electronic and optoelectronic behaviour. We use the technique to assemble twisted-graphene heterostructures in ultra-high vacuum, resulting in a tenfold improvement in moiré superlattice homogeneity compared to conventional transfer techniques.

Van der Waals (vdW) heterostructures—artificial materials composed of a sequence of specified two-dimensional (2D) materials—can be used to create unique electronic and optoelectronic devices with atomically sharp and clean interfaces[1,2]. The fabrication of these heterostructures typically relies on the mechanical stacking of individual 2D material crystals. The wide variety of polymer-assisted transfer approaches[3] can generally be categorized into two groups: 'wet' transfer, in which the 2D materials come into direct contact with liquid[4,5], and 'dry' transfer, in which the surface remains dry throughout the transfer process[6]. These techniques are used to pick up grown[4,7–9] or exfoliated 2D crystals[5] and assemble them into multilayer stacks[10,11]. All these approaches use a polymer support to manipulate the vdW heterostructure before the

[1]Department of Physics and Astronomy, University of Manchester, Manchester, UK. [2]National Graphene Institute, University of Manchester, Manchester, UK. [3]Department of Materials, University of Manchester, Manchester, UK. [4]Materials Department, Imperial College London, London, UK. [5]National Institute for Materials Science, Ibaraki, Japan. [6]Graphene Engineering Innovation Centre, University of Manchester, Manchester, UK. [7]Department of Physics, University of Lancaster, Lancaster, UK. [8]Henry Royce Institute for Advanced Materials, University of Manchester, Manchester, UK. [9]These authors contributed equally: Wendong Wang, Nicholas Clark, Matthew Hamer, Amy Carl. ✉e-mail: nick.clark@manchester.ac.uk; alex.summerfield@manchester.ac.uk; roman@manchester.ac.uk

stack is complete and deposit it onto a substrate compatible with the desired function of the final device.

However, the polymer supports used in the 2D transfer and stacking process are a source of interlayer contamination. Achieving 2D heterostructures that behave as artificial crystals, rather than independent materials, requires atomically clean interfaces. Transistors and light-emitting devices fabricated from vdW heterostructures operate well only in areas that are free from contamination[3]. The ballistic transport of charge carriers, which is important for many fundamental physics experiments, is achieved only in the limit of extreme cleanliness[12]. Although the polymer layers have excellent adhesion and flexibility, their residues remain at buried interfaces or on the surface of the completed heterostructure, depending on the method used[3]. Another source of surface and interfacial contamination is volatile species from the surrounding environment condensing onto surfaces before and during the stacking process. A route to avoid this would be to process in a high or ultra-high vacuum (UHV) environment, but this is not compatible with polymer transfer approaches due to outgassing from the polymer. Consequently, vdW heterostructures are currently assembled in air, inert gases[13,14] or low vacuum[15].

The strong adhesion between 2D materials causes contaminants to aggregate into localized pockets known as blisters or bubbles[8,12,16], which consist of air, water and hydrocarbons[2,16,17]. The localized contamination limits the size of homogeneous regions with atomically clean interfaces[18] to micrometres, restricting the experiments that can be performed and hampering the development of electronic applications for which large uniform areas are required. For graphene and hexagonal boron nitride (hBN) heterostructures, the diffusion of surface contaminants can be promoted by performing transfers at elevated temperatures (for example, at around 110 °C) and gradually collapsing the contact front of the polymer (a 'slow transfer')[16], which prevents contaminants from being trapped at the interface as it is formed. However, the use of polymer supports limits the permitted temperature to under around 150 °C (depending on the glass transition temperature of the polymer), thus forbidding the higher temperatures that could facilitate the formation of large-area heterostructures for many 2D materials. It also prevents some methods, such as aggressive cleaning techniques, being used to improve cleanliness (for example, most organic solvents will swell or dissolve the polymers used).

There are strategies for removing the contamination from already assembled heterostructures[18,19]. However, the cleaning processes are slow even for micrometre-scale devices, cannot be widely adopted and risk damaging the structure due to the excessive heat or high mechanical stresses involved. Furthermore, some 2D materials undergo chemical degradation during exfoliation and transfer in ambient environmental conditions[3,20]. This problem is often mitigated by operation in pure argon or nitrogen atmospheres[13,14]. However, even in a state-of-the-art inert glovebox environment, some atomically thin crystals, such as CrI_3 and monolayer InSe (ref. 21), will still degrade due to residual oxygen and water.

In this article, we report a platform for fabricating clean 2D material heterostructures without using any organic materials. An inorganic flexible silicon nitride (SiN_x) membrane covered with thin metallic films is used as a replacement for the polymer layer in the transfer process. The metal film thickness and composition can be changed to tune the adhesion properties, enabling high transfer reliability with nearly 100% yield for a wide range of 2D materials. The approach provides additional flexibility in the transfer conditions, including assembly in UHV at a pressure of ~10^{-10} mbar. We show that the technique can be used with transfers in air, gloveboxes or UHV environments at temperatures up to 350 °C, enabling reliable fabrication of devices with clean areas limited only by the size of the crystals used. Graphene devices created using the technique exhibit carrier mobilities over 10^6 cm^2 V^{-1} s^{-1} at 4 K. We also demonstrate a large increase in the size of atomically clean areas of complex multilayer heterostructures and enhanced moiré uniformity in twisted devices compared with those previously reported, as well as the scalable transfer of chemical vapour deposition (CVD)-grown materials. Our technique could potentially remove the cleanliness bottlenecks in 2D material nanofabrication and provide scale-up pathways[22,23].

Inorganic assembly in air or a glovebox

The transfer relies on chemically inert, flexible and transparent SiN_x membranes. For smaller heterostructures built from mechanically exfoliated crystals with lateral dimensions of tens of micrometres, the membranes are typically shaped into cantilevers, each 320–480 μm long by 160 μm wide protruding from a silicon chip (Fig. 1a). These are fabricated at wafer scale using commercially available silicon wafers coated with 500 nm low-pressure CVD-grown SiN_x on both sides. Optical lithography and reactive ion etching are used to pattern the nitride layers into the required cantilever geometry before wet etching is used to selectively remove the underlying silicon and release the cantilevers (Supplementary Section 1).

The strong adhesion between the 2D materials and the polymer support layers is the key factor that has made polymer-based transfer methods universal. In comparison, bare SiN_x has poor adhesion to 2D materials. To address this problem, we coat the cantilevers with a tri-metal stack consisting of 1 nm Ta, 5 nm Pt and 0.1–1.0 nm Au (Fig. 1b–d). Gold generally has strong adhesion to 2D materials[24,25] but adjusting its thickness allows us to tune the adhesion strength for a specific 2D/substrate combination (a higher gold surface density leads to stronger adhesion). This is highly beneficial as it allows the completed heterostructures to be released onto various substrates once the desired layer combination is assembled. The role of the Pt layer is to compensate for the variable SiN_x roughness and ensure consistent surface quality between different SiN_x substrates. Additionally, the presence of Pt facilitates the catalytic decomposition of mobile surface hydrocarbons[26] at elevated temperatures. The Ta serves as the adhesion layer for Pt. Figure 1e is an atomic force microscopy (AFM) image showing the roughness of the cantilever surface. The typical root-mean-square deviations are 130–140 pm. Energy dispersive X-ray spectroscopy (EDX; Supplementary Fig. 10) shows the uniform distribution of all three metals across the surface, which is not the case if the Pt layer is removed due to the tendency of Au to form nanoclusters.

We benchmark this transfer approach by demonstrating the high cleanliness achievable for the archetypal hBN/graphene/hBN vertically stacked heterostructure, fabricated from mechanically exfoliated 2D crystals on an Si/SiO_2 substrate. As illustrated in Fig. 1f, the commercial 2D crystal transfer set-up (Methods) is used to align the custom cantilever over a target hBN crystal (Fig. 1g). The cantilever is lowered with a 20° tilt until contact is made at 120–150 °C. The cantilever is raised after a few seconds, peeling the crystal away from the substrate (Fig. 1h). The optimal gold thickness for transferring most 2D materials onto SiO_2 is 0.65 nm, with >95% successful transfers for over 200 operations. The cantilever with the hBN attached is then used to pick up the next layer in the heterostructure (graphene, as shown in Fig. 1i,j) and the resulting stack is then deposited onto the bottom hBN (shown in Fig. 1k) by exploiting the greater adhesion to this larger bottom crystal. The lamination process is stopped before the entire bottom hBN crystal is covered by the cantilever to selectively release the stack instead of picking it up. Figure 1o shows an optical micrograph of the finished stack consisting of a large clean region with no contamination or bubbles over an area larger than 25 μm × 40 μm, which has been formed despite a very fast (few seconds) lamination speed. Additional stacks are shown in Extended Data Fig. 1. The absence of polymers during the processing allows for much higher temperatures. For the stack in Fig. 1, we used 150 °C for the first hBN, 120 °C for the graphene and 230 °C for the second hBN. For transfers in air or inert gas, we have tested transfer temperatures up to 300 °C and observed the complete disappearance of hydrocarbon bubbles above ~220 °C. However, heating above 150 °C

https://doi.org/10.1038/s41928-023-01075-y

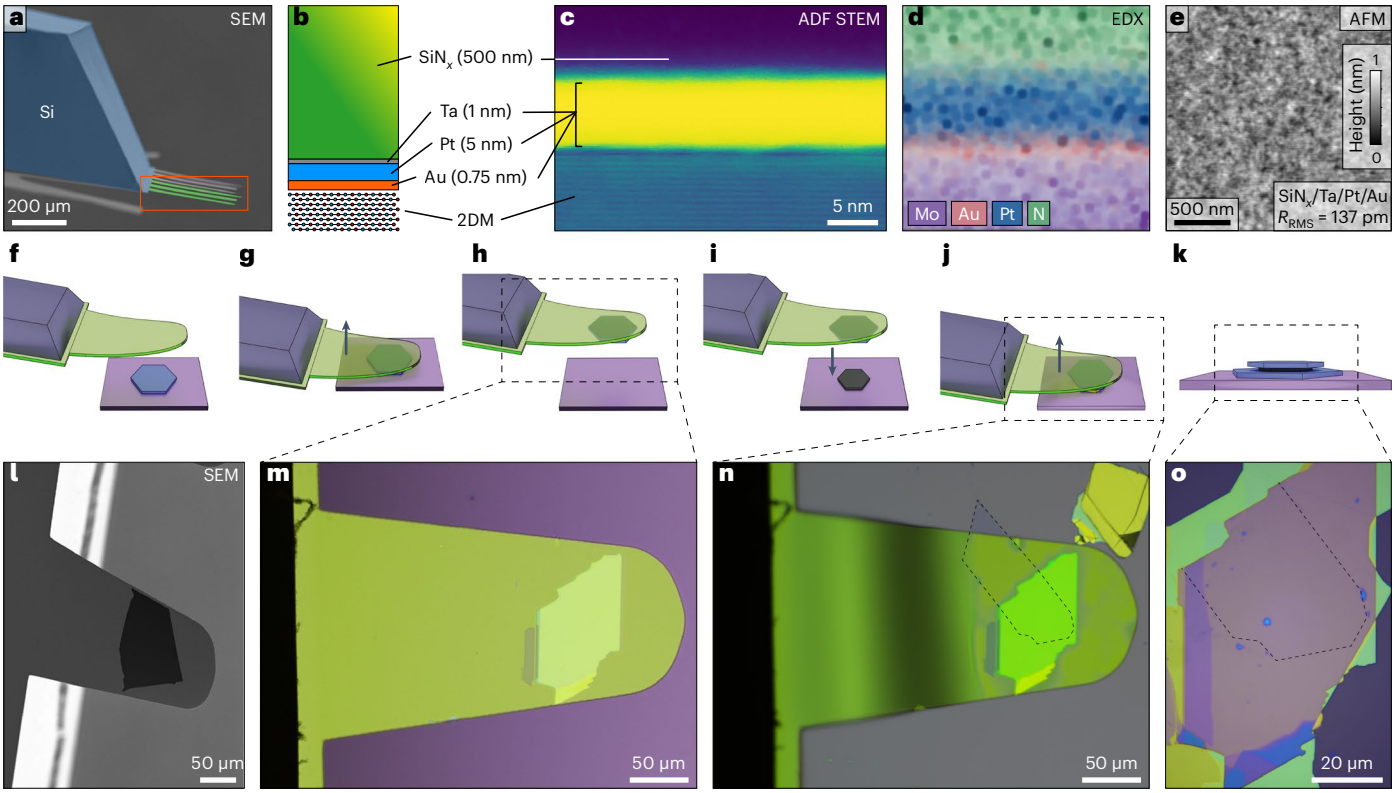

Fig. 1 | Inorganic assembly of vdW heterostructures. a, Scanning electron microscopy (SEM) micrograph of several cantilevers protruding from a silicon chip. **b**,**c** Schematic (**b**) and cross-sectional annular dark-field (ADF) scanning transmission electron microscopy (STEM) image (**c**) showing the multilayer metallic coating of the cantilever holding a 2D material (2DM) specimen (sample shown is a multilayer MoS_2 crystal). **d**, Elemental mapping of the region in **c** using EDX. **e**, AFM micrograph of the cantilever surface after the coating process. The root-mean-square (RMS) roughness values are indicated on the image. **f**–**h**, Steps employed to pick up an hBN crystal onto the fabricated cantilever: alignment (**f**), contact (**g**) and lift-off (**h**). **l**,**m**, SEM (**l**) and optical (**m**) micrographs of the cantilevers after picking up thick (~40 nm) hBN crystals. **i**,**j**, Steps involved in picking up a graphene crystal: alignment (**i**) and contact and lift-off (**j**). **n**, Optical micrograph showing the cantilever in contact with graphene (edges highlighted with a dashed line) on SiO_2. The flexible nature of the cantilevers allows accurate control of the lamination process. **k**, Graphene/hBN stack deposited onto the bottom hBN crystal. **o**, Optical micrograph showing the resulting heterostructure on an oxidized silicon wafer with large uniform areas. Further data on additional samples can be found in Extended Data Figs. 1 and 2.

in argon during the picking up of monolayer graphene from SiO_2 may produce microcracks in the graphene, presumably due to the increase in the adhesion of graphene to SiO_2 (ref. 27) and vibrations of the cantilever (see Supplementary Section 2 for details). A further advantage of our approach is the improved positioning accuracy compared to polymer-based methods. This is limited only by the optical resolution of the microscope used (better than 400 nm), as the inorganic SiN_x membrane displays negligible drift and warping when heated and compressed (Supplementary Video). After the transfer, the membranes can be cleaned in Ar/O_2 plasma and reused several times.

To characterize the quality of the encapsulated graphene, we fabricated five multi-terminal Hall bar devices with various dimensions in an argon environment and studied them at 4 K. For three of the samples, which each had a width ≤12.5 μm, we found that the carrier mean free path l was limited by their physical dimensions and that the field-effect mobility (Fig. 2a) followed the characteristic dependence $\mu = l(2e/h)\sqrt{\pi/n}$, where e, h and n are the elementary charge, Planck constant, and carrier concentration, respectively, reaching well over 10^6 cm^2 V^{-1} s^{-1} at low carrier concentrations. This behaviour is typical for current state-of-the-art devices whose Hall bar dimensions are limited to 20 μm when using polymer transfer[10,28,29]. However, for a larger device, with dimensions 38 μm × 33 μm, we do not see such saturation. In fact, the carrier mobility increases with carrier density, reaching up to ~3×10^6 cm^2 V^{-1} s^{-1}. This behaviour suggests that a different scattering mechanism becomes relevant for large devices, probably related to carbon and oxygen substitutional impurities intrinsically present in the hBN encapsulation, which varies between different crystals exfoliated from the same growth batch[30].

Despite previously reported demonstrations of heterostructure devices with strong proof-of-principle optoelectronic performance, the random network of contamination bubbles on micrometre scales means that the promises of such applications are unrealistic. Electronic-grade materials require nearly 100% areal uniformity for the design of the dense circuit elements such as optical emission arrays or transistors, which makes even simple heterostructures, such as polymer-assembled encapsulated graphene, unusable for high-end electronic applications. Even more challenging are applications for multilayer heterostructures containing 2D semiconductors, such as vertical light-emitting devices[11,31], which typically have very small clean areas (<2 μm × <2 μm, with over 50% of their area covered by contamination bubbles) and take several days or weeks to fabricate. Here, we assemble a complex structure consisting of eight individual 2D layers with different thicknesses ranging from bulk to a monolayer. The optically active layers are two twisted few-layer molybdenum disulfide (MoS_2) crystals (outlined with the yellow and orange dashed lines in Fig. 2b). The entire heterostructure, fabricated in an argon atmosphere, has no bubbles and has a completely clean 9 μm × 15 μm area where all eight layers overlap, as confirmed by overall AFM and local cross-sectional STEM measurements (Fig. 2c,d). A comparison of the topography with that of five similar devices fabricated using

https://doi.org/10.1038/s41928-023-01075-y

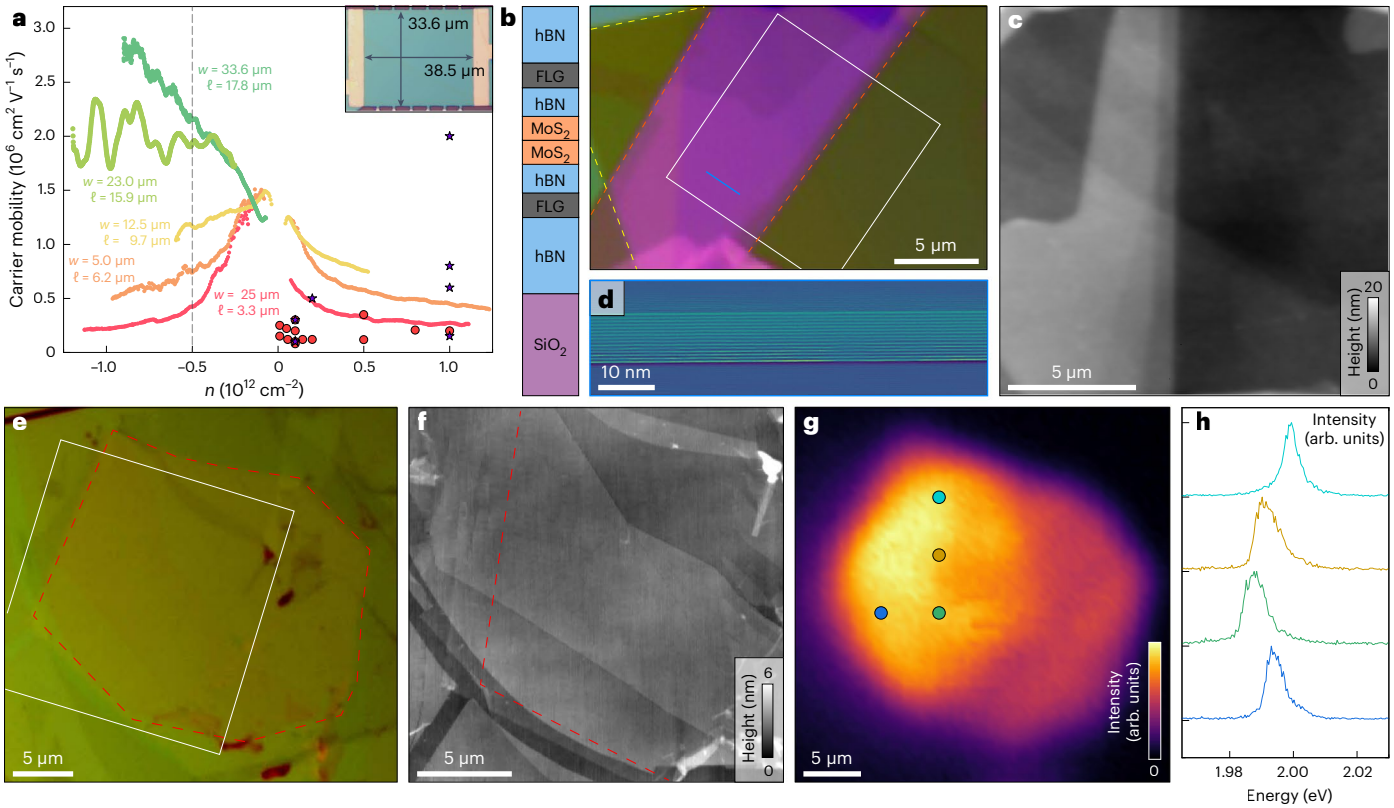

Fig. 2 | Heterostructures assembled using our fully inorganic transfer technique in air and argon. a, Carrier mobility at 4 K for five graphene devices. For large channel dimensions (>20 μm), some samples display unusual trends, unlike that expected from the edge scattering. For smaller devices, the extracted values of the carrier mean free path l agree well with the dimensions of the studied devices as indicated by the width, w. Points indicate mobility values (calculated using the Drude relation) acquired from the published literature when polymeric transfer has been used. Purple stars correspond to samples fabricated at Manchester University and red circles by other groups (see Supplementary Table 1 for full details). **b**,**c**, Optical (**b**) and AFM micrographs (**c**) of an eight-layer stack assembled in air. Layer sequence is shown on the left. FLG, few-layer graphene. No bubbles are present, although some crystals folded during the pick-up process. **d**, Cross-sectional HAADF-STEM image showing the cross section of the device at the location marked with the blue line in **b**. Graphene and hBN layers are indistinguishable due to their close atomic masses. Local contrast enhancement has been applied to the image to highlight the layered structure. **e**,**f**, Optical (**e**) and AFM (**f**) micrographs of a light-emitting diode-type structure[11] with monolayer WS_2 selected as the optically active layer. **g**, Electroluminescence intensity map for the device in **e**, showing a highly uniform emission distribution with a pronounced terraced structure due to variation in the hBN barrier thickness (three to five layers). **h**, Example of electroluminescence spectra acquired for the points labelled in **g**.

polymer-based transfer techniques in the same atmosphere is presented in Supplementary Fig. 4. Up to half of the active area of each of these five devices is occupied by a dense network of contamination bubbles. The absence of contamination can also be seen in another light-emitting structure assembled using an SiN_x membrane (Fig. 2e,f), which features monolayer tungsten disulfide (WS_2) as the optically active layer. Its electroluminescence emission demonstrates that it has an ultraclean overlap area of 25 μm × 30 μm. Both assemblies took only 10 min to complete and resulted in over a 100-fold increase of the uniform heterostructure area compared to the polymer-assembled structures, limited in this instance only by the size of the exfoliated crystals. When a bias voltage is applied to the graphene layers, we observe a bright uniform electroluminescence signal with a terrace-like distribution of the intensity across the device (Fig. 2g), which is related to the change in thickness of the tunnelling hBN layers. Narrow exciton emission lines (4–5 meV) confirm the state-of-the-art optoelectronic quality of the device (Fig. 2h), which is like that recently reported for small samples[32]. A slight variation in the emission energy across the device is commonly attributed to the non-uniform impurity distribution in the original crystal[33]. This exemplifies the importance of our technique, as the advanced optical performance, previously observed only at selected specimen locations ~2 μm large, can now be realistically considered in the context of advanced applications.

The transfer process that we have developed was also tested for a variety of air-sensitive 2D materials that require fabrication in an argon environment (for example, black phosphorus, WSe_2 and $NbSe_2$) exfoliated onto different substrates, including SiO_2 and polymers such as poly(methyl methacrylate) (PMMA) and polypropylene carbonate spin-coated onto Si wafers. In all the cases, we observed the complete absence or considerable reduction in the presence of hydrocarbon pockets (Extended Data Fig. 2a–c). Lithographically patterned 2D crystals can also be transferred (Extended Data Fig. 2d,e). However, note that some dry-etching processes lead to chemical bonding of the 2D crystals to the substrate surface along the etched perimeter.

Previous work has shown improved heterostructure device performance when the transfer is performed in organic solvents to reduce wrinkling and strain[34,35]. However, these experiments were limited to polymer-compatible solvents (alcohols and alkanes). In contrast, our fully inorganic transfer method allows transfers even when the sample is submerged in almost any organic solvent, for example ketones or chloroform, which are more likely to effectively remove contamination[27,36] during the transfer. Indeed, we have confirmed that the transfer also works in a variety of organic solvents incompatible with the polymer-based transfer method (toluene, chlorobenzene, cyclohexane, chloroform, various ketones, etc.), although in some cases, mostly for polar solvents, a second micromanipulator was required to push the

https://doi.org/10.1038/s41928-023-01075-y

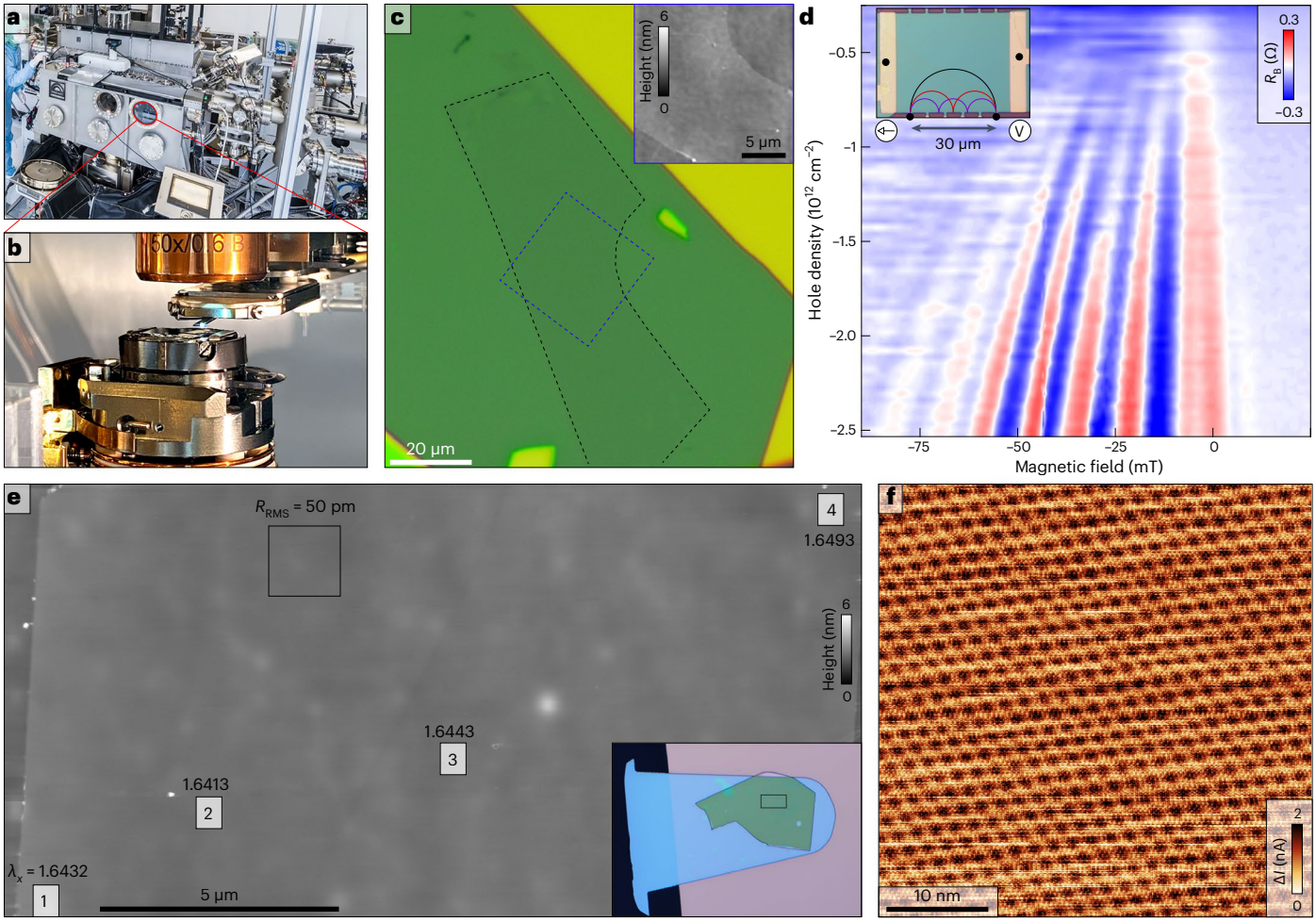

Fig. 3 | UHV assembly of vdW heterostructures. a, Instrument for performing UHV assembly allowing 15-axis manipulation for the 2D material transfer and including an integrated optical microscope. **b**, Close-up of the optical lens, cantilever and sample stage. **c**, Example of a UHV-fabricated vdW heterostructure: hBN-encapsulated graphene on graphite (serving as a local back gate). The graphene is outlined with a black dashed line. No hydrocarbon contamination can be observed over the entire sample. The inset shows a 25 μm AFM scan of the area highlighted by a blue dashed box. **d**, Magnetic focusing experiment performed at 5 K on a similar heterostructure as in **c**, indicating ballistic transport on the scale of >30 μm, corresponding to a carrier mobility over 6×10^6 cm^2 V^{-1} s^{-1}. The inset is a schematic of the measurement process. Electrons injected from one contact are magnetically deflected into the other contact (the collector) while the corresponding voltage is measured. The transfer resistance displays several focusing peaks, with the first peak corresponding to the direct transfer of electrons from the injector to the collector. The subsequent peaks (at higher magnetic field) are produced when the electrons scatter from the edge of the device before reaching the collector. **e**, AFM topography map of a twisted-graphene monolayer/bilayer heterostructure placed on a bulk hBN crystal. Numbers give the x component of the moiré period extracted at the indicated locations using c-AFM measurements. Small white bead-like objects are gold clusters resulting from contact deposition using a stencil mask. The elevated areas are the protruding roughness of the SiN_x support. The inset is an optical micrograph of the stack on the cantilever broken on the edge of a silicon wafer. **f**, Example of c-AFM micrograph collected from the sample shown in **e** and used for the moiré period analysis.

cantilever down to touch the substrate, presumably due to the formation of a repulsive solvent shell on the solid surfaces. An example of this process performed in acetone can be found in Extended Data Fig. 2g–i.

UHV assembly

Further improvements in vdW cleanliness are limited by atmospheric contamination[37]. To eliminate the interlayer contamination completely, we designed and built a 15-axis micromanipulation set-up enclosed within a UHV chamber, with a base pressure of 4×10^{-10} mbar (Fig. 3a). The heterostructure assembly followed the procedure described in Fig. 1 using a custom-built UHV optical microscope integrated into the UHV chamber. Further details of the UHV system design can be found in Supplementary Section 4.

There are no contamination bubbles across the entire interface of the vdW heterostructures fabricated under UHV (Fig. 3c), regardless of the transfer speed and crystal dimensions. Electronic transport measurements for an example vdW heterostructure, comprising hBN/graphene/hBN, show ballistic transport over a scale of ~40 μm, as seen in magnetic focusing experiments[38] (Fig. 3d), and a field-effect mobility of ~3×10^6 cm^2 V^{-1} s^{-1} (at $n = 0.5 \times 10^{12}$ cm^{-2}). To achieve this, all 2D crystals on Si/SiO_2 substrates introduced to the chamber went through UHV annealing at 400 °C and were assembled into heterostructures at 150 °C (Fig. 3b). We found that higher conditioning temperatures (600 °C) resulted in a noticeable decrease in the low-temperature mobility of graphene ($\mu < 4 \times 10^5$ cm^2 V^{-1} s^{-1} in four samples studied). Although the hBN-encapsulated graphene is immune to degradation at high temperatures[39], annealing on the Si/SiO_2 substrate may lead to local damage to the graphene lattice.

This extreme cleanliness is possible only when polymer-free transfer and UHV conditions are combined. To verify this, we fabricated

https://doi.org/10.1038/s41928-023-01075-y

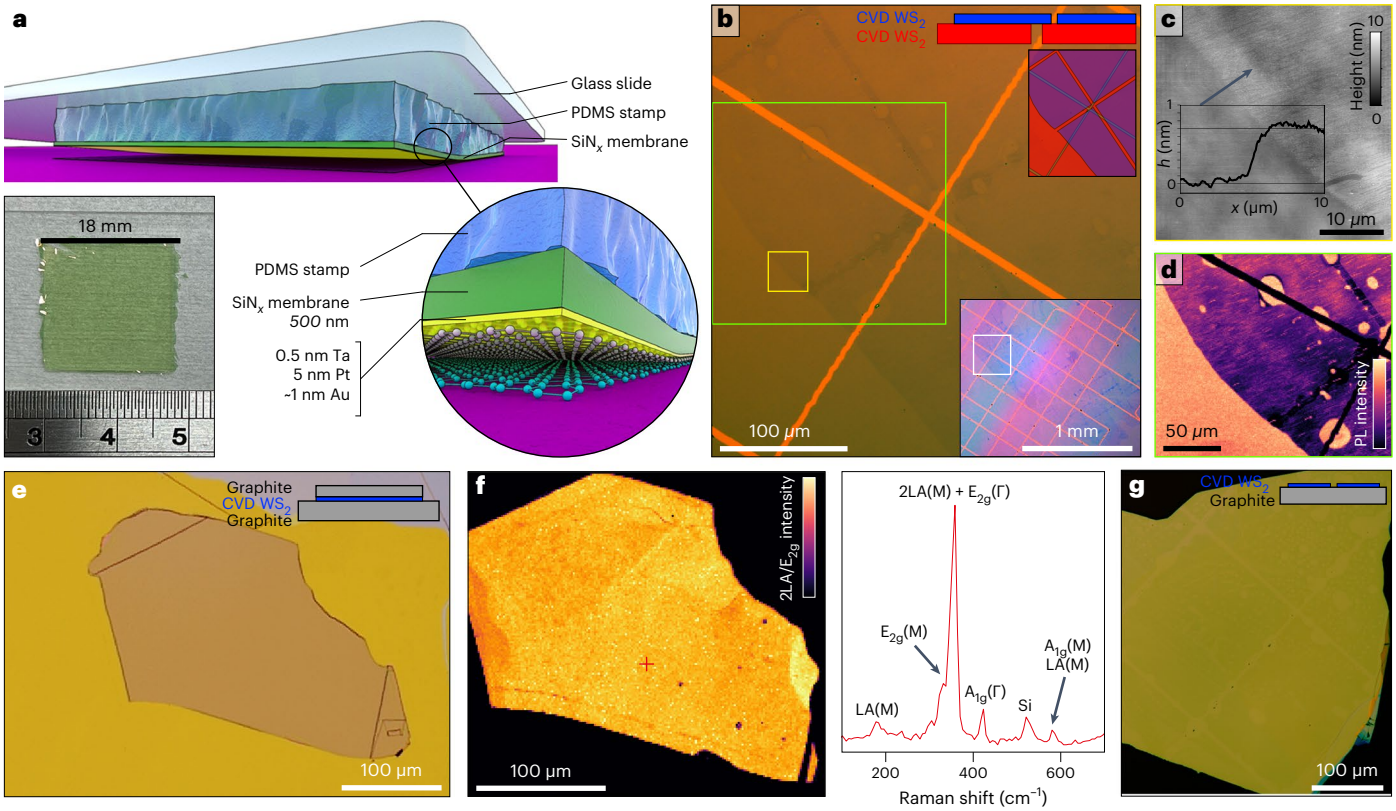

Fig. 4 | Large-area transfer of CVD-grown 2D materials. a, Schematic showing the arrangement of an SiN_x membrane supported by PDMS polymer. The inset shows an 18 mm SiN_x membrane laminated onto PDMS film. **b**, Heterostructure consisting of CVD-grown monolayer WS_2 transferred onto CVD-grown few-layer WS_2 on an SiO_2 substrate fabricated using the laminates shown in **a**. A square grid was scratched into both layers before the transfer to enable visualization. The upper inset shows the two layers in red and blue to highlight the areas covered. The lower inset shows a wider view, with the location of the main image indicated by the white box. **c**, Topography of the area in **b** indicated by the yellow rectangle. A height profile at the indicated position is shown in the inset, measuring a step of approximately 0.7 nm. **d**, Integrated intensity map of the primary WS_2 photoluminescence (PL) peak around 1.97 eV. **e**, A thin WS_2 layer encapsulated in thick graphite fabricated using the large-area stamping method. **f**, Map of the intensity of the WS_2 $2LA/E_{2g}$ Raman peak normalized by the Si peak and a representative Raman spectrum from the location indicated by the red cross. **g**, CVD-grown WS_2 monolayer transferred onto a mechanically exfoliated graphite crystal. A square pattern has been scratched into the WS_2 monolayer to enable visualization.

similar hBN/graphene/hBN heterostructures in UHV but using the traditional transfer technique with a small hemispherical PMMA droplet deposited onto a glass slide instead of the SiN_x cantilever (Supplementary Section 6). Despite using an analogous annealing protocol, there was a considerable number of hydrocarbon pockets in the heterostructures. This indicates that the use of polymer makes contamination unavoidable, even in a UHV environment, since the loose polymer matrix can emit hydrocarbons after prolonged temperature treatment and pumping.

In addition, we demonstrate the applicability of the fully inorganic transfer approach in a UHV environment for producing twisted vdW heterostructures. The perfect cleanliness leads to exceptional uniformity, opening opportunities for new experimental studies. The ability to exploit a small local twist between neighbouring 2D materials to generate new physics is one of the degrees of freedom not seen in other types of synthesis. Yet the understanding and exploitation of the properties of such structures are held back by the poor specimen uniformity, with micrometre-sized areas often displaying local variations in twist angle up to 0.2°, resulting from wrinkles present due to contamination bubbles[40]. In twisted bilayer graphene, this variation leads to difficulties in studying strongly correlated phenomena such as superconductivity[41] and magnetic states[42], which are extremely sensitive to twist angle disorder. We have used our fully inorganic UHV assembly to fabricate a twisted monolayer/bilayer graphene on a thick hBN substrate.

AFM topography of the fabricated twisted bilayer reveals no contamination bubbles over the entirety of the heterostructure (Fig. 3e). Additionally, conductive AFM (c-AFM) measurements reveal that the moiré period of the superlattice is exceptionally uniform (Fig. 3f), with the extracted twist angle $\theta \approx 8.5°$, varying by just 0.016° over a length scale of 10 μm (areas labelled 1, 2 and 3 in Fig. 3e), and within 0.04° for the entire area shown. This result represents an order of magnitude improvement compared to the twist angle disorder achieved with polymer-based transfer techniques.

Scalability of the SiN_x transfer method

The cantilever geometry can also be used to transfer CVD-grown materials, as exemplified in Supplementary Fig. 3, where WS_2 monolayer crystals[43] have been picked up from their growth substrate (SiO_2) and encapsulated in hBN. However, the free-standing nature of the 500-nm-thick SiN_x makes it difficult to apply this technique over lateral scales larger than ~200 μm. To overcome this problem, we have laminated a metal-coated SiN_x membrane onto a 0.432-mm-thick polydimethylsiloxane (PDMS) film (Fig. 4a). Direct contact of the 2D crystals with the PDMS surface produces surface contamination[44] due to the presence of uncrosslinked oligomers within the PDMS bulk. However, the SiN_x membrane provides an impermeable barrier for this contamination, allowing us to combine both the ultraclean interface of the metallized SiN_x with the mechanical flexibility and support of PDMS, thus enabling greatly expanded contact areas (up to 6 cm^2, as

shown in Extended Data Fig. 3d,e). This arrangement has allowed us to pick up a large CVD-grown WS_2 sheet from its growth substrate (SiO_2) and deposit it onto multilayer WS_2 films grown on sapphire and SiO_2 substrates. The resulting heterostructure, shown in Fig. 4b, exhibits no bubbles. The AFM-measured step height of the top layer is 0.7 ± 0.1 nm AFM step height. Together, these suggest that there is an absence of contamination in the interface, which is consistent with the 50–60% reduction in the photoluminescence intensity in the overlapping area (Fig. 4d). A wider view of the stack in the inset in Fig. 4b and Extended Data Fig. 3 shows that the area transferred is over 1 mm^2 and is limited by inhomogeneities in the original material (Extended Data Fig. 3b) rather than the transfer method. Despite the use of PDMS, we are still able to perform transfers at 250 °C, though other grades of PDMS allow for higher working temperatures (for example 350 °C)[45].

However, we found that the roughness of the growth substrate plays an important role. Although the process works for flat substrates with subnanometre root-mean-square height variance (for example, SiO_2/sapphire), we had difficulties picking up commercially produced graphene grown on copper foil as its roughness reaches micrometre scale, thus preventing the uniform contact of the SiN_x membrane with the graphene. However, recent developments in growing ultra-flat metallic surfaces and their use as substrates for the CVD growth of 2D materials[46–48], optimizing growth processes for increased large-scale uniformity[49,50] and improvements in direct growth on flat non-metallic substrates[51] should allow the use of inorganic transfers when the materials are made widely available. Further information and a critical discussion on the scalability of this technique are included in Supplementary Section 3.

Conclusions

We have reported an inorganic 2D material transfer technology using metal-coated silicon nitride membranes that avoids the use of polymer layers. The process can improve the cleanliness, uniformity and quality of vdW heterostructures assembled in air and inert gases, and it allows assembly to be performed in a UHV environment. Using this approach, we assembled an hBN/graphene/hBN Hall bar with an area over 1,200 μm^2 and a field-effect mobility up to 3×10^6 $cm^2 V^{-1} s^{-1}$, a multilayer light-emitting device with an optically active area of ~750 μm^2 and a large-area twisted bilayer graphene sample with a highly uniform moiré superlattice. We also transferred air-sensitive 2D materials, pre-patterned crystals and CVD-grown materials directly from their growth substrates. The SiN_x films used are already commercially available at wafer scale and possess superior chemical, thermal and mechanical stability compared to organic polymers. Our transfer method enables the fabrication of highly uniform vdW heterostructure devices for which performance is limited only by the intrinsic quality and dimensions of the 2D crystals.

Although the free-standing SiN_x cantilevers described here are more suitable for small-scale research applications, the technology relies on the general properties of the SiN_x/metal surface and could be used to create large-area laminates, thus providing a potential pathway to the wafer-scale transfer of sufficiently flat CVD materials. In addition, compatible alternative pathways to scale up have been developed using autonomous robotic searching and assembly of 2D crystals[22,23]. We envisage that due to the high reproducibility, cleanliness and speed offered by our technique, in combination with machine learning algorithms to guide[52] the decision-making process, it can be used for small-scale manufacturing of custom high-end optoelectronic devices for applications in which large batch production is not required, such as quantum technologies, aerospace and healthcare.

Methods

SiN_x cantilever fabrication

SiN_x transfer cantilevers were fabricated from silicon wafers coated on both sides with low-stress (non-stoichiometric) SiN_x films, purchased from Inseto UK. The nitride layers on either side were patterned using optical lithography and subsequent reactive ion etching to define both the cantilevers and a hard mask for anisotropic etching of the Si. Potassium hydroxide solution was then used to remove the silicon from the area defined by the SiN_x mask. After cleaning, the metallic adhesion layer was deposited using direct sequential sputtering of Ta and Pt, followed by e-beam deposition of Au immediately before use. See Supplementary Section 1 for the full details.

SiN_x laminate fabrication

Rectangular SiN_x membranes were fabricated from silicon wafers coated on both sides with 500-nm-thick low-stress (non-stoichiometric) SiN_x films, purchased from Inseto UK. The nitride layer on one side was patterned using optical lithography and subsequent reactive ion etching to define a hard mask for subsequent anisotropic etching of the Si, leaving a free-standing SiN_x membrane on the other side. To support the SiN_x membrane, a rectangular PDMS sheet, thickness 0.432 mm (Medium Tack DGL film grade X4, Gel Pak) was cut to a size slightly smaller than the SiN_x window and carefully placed onto a clean transparent supporting substrate before being brought into contact with the nitride window at a temperature of 150 °C and held for a few seconds. When the glass substrate is pulled away, it carries the SiN_x membrane, with the membrane fracturing along its edge under strain. The membrane was then metallized by sequential sputtering of the Ta and Pt layers, before e-beam evaporation of the thin Au layer. See Supplementary Section 3 for the full details.

2D heterostructure fabrication with cantilever geometry

2D crystals were mechanically exfoliated onto oxidized silicon wafers. For assembly in air or argon atmosphere, cantilevers were used to pick up and drop off 2D crystals using a standard micromanipulator system[3] with a temperature-controlled stage. For UHV assembly, exfoliated crystals were loaded into a custom UHV system and annealed in a load-lock (pressure ~10^{-7} mbar) before being introduced into the main UHV chamber (pressure ~10^{-10} mbar) to remove atmospheric hydrocarbon contamination and adsorbed H_2O. Separately, a metal-coated SiN_x cantilever was loaded and annealed before its introduction into the main chamber through the same load-lock. After annealing, the cantilevers (substrates) were loaded into the top (bottom) precision manipulators using a combination of linear and 'wobble-stick' style UHV manipulator arms. For stacking operations, the manipulators were controlled using a custom LabView-based program with the substrate/stamp positioned underneath an array of UHV objective lenses (×5/20/50/100 magnification) for inspection and precise alignment of the 2D crystals. A cantilever and the 2D crystals were brought into contact at an elevated substrate temperature, ~150 °C, to form the heterostructure stacks. Between each stacking step, the partially assembled heterostructure was annealed to remove surface contaminants. Full technical details of the UHV transfer procedure and system, together with the annealing recipes for each step, can be found in Supplementary Sections 4–6.

2D heterostructure fabrication with laminate geometry

To fabricate large-area heterostructures, we utilized CVD-grown WS_2 on SiO_2 (290 nm thick) and sapphire substrates. This encompassed both individual triangular structures and continuous films. CVD-grown WS_2 triangles or continuous WS_2 films were gently picked up at 150 °C within an argon glovebox using the equipment described in the previous section. Then, we dropped off the picked-up CVD flakes from the SiN_x membrane to alternative CVD substrates or exfoliated flakes, such as graphite or hBN, at a temperature of 250 °C.

Transport device fabrication

After assembly, hBN/graphene/hBN stacks were dropped from the cantilever onto a large graphite crystal (50–100 nm thick) pre-exfoliated

onto a Si/SiO_2 wafer and were used for applying the back gate. The hBN/graphene/hBN/graphite heterostructures were processed into standard Hall bar devices using e-beam lithography and reactive ion etching. Electrical contacts consisting of 3 nm Cr and 70 nm Au were affixed onto the graphene with the one-dimensional technique[8]. Electrical measurements were performed at a temperature 5 K using the standard lock-in technique.

UHV c-AFM device fabrication

Twisted-graphene samples for c-AFM were fabricated using the tear and stack method[53]. First, a large hBN crystal was picked up on a cantilever. Graphite was mechanically exfoliated onto an oxidized silicon wafer and monolayer/bilayer graphene crystals were identified using optical contrast. The hBN crystal on the cantilever was lined up with the edge of the bilayer section of the graphene crystal and slowly brought into contact with the surface. The cantilever was then picked up, ripping the graphene along the edge of the hBN crystal. The section of graphene crystal remaining on the substrate was then rotated to the desired angle, realigned with the first half already on the cantilever and picked up. The cantilever with the hBN/bilayer graphene/graphene heterostructure was then flipped upside down and broken off onto the edge of a SiO_2 wafer coated with a metallic adhesion layer (2 nm Ti and 20 nm Au) such that the twisted-graphene surface was exposed. To ensure a reliable electrical contact during the c-AFM measurements, a stencil mask was used to deposit a 150 nm Au film contacting the graphene.

Atomic force microscopy

AFM topography of fabricated heterostructures was measured in a.c. mode using a Dimension Icon (Bruker Nano) system in a clean room and a Cypher-S (Oxford Instruments) system in an argon environment. c-AFM maps were acquired of twisted-graphene samples deposited on top of hBN flakes using a Cypher-S AFM (Oxford Instruments) in an argon environment. c-AFM maps were acquired in contact mode with a constant tip–sample potential difference of −50 mV and a scan rate 1.5–1.75 Hz. The local twist angles were calculated from the component of the moiré wavelength along the fast-scan direction to minimize the effect of temporal drift. Periodograms[54] were calculated for each scanning line and then summed along the slow scan axis to generate a magnitude spectrum in the fast direction. Peaks identified in the spectrum were then fitted with Gaussian functions to measure the peak frequencies and, therefore, the spatial periodicity. If the high-symmetry direction of the moiré lattice was not aligned with the fast-scan axis, we calculated the angle withstood by both directions α and then applied a trigonometric transformation to obtain the period of the moiré lattice and, therefore, the local twist angle. Full details are supplied in Supplementary Section 7.

Cross-sectional STEM and EDX

Cross-sectional samples were prepared using a focused ion beam with decreasing currents to mitigate beam damage induced during milling. Image data and elemental maps were acquired on a FEI Titan G2 80-200 S/TEM with a four-quadrant Super-X EDX detector, operating at 200 kV accelerating voltage. The annular dark-field STEM data were acquired with a probe current of 180 pA, a semi-convergence angle of 21.5 mrad and an inner angle of 43 mrad for the annular dark-field detector. EDX mapping was performed using the same probe conditions, with a pixel dwell time of 40 µs. In the map shown in Fig. 1d, individual X-ray counts are plotted as circles according to the colour scheme shown in the image. Both Mo and S counts are included as Mo due to the overlap of the peaks. Further details can be found in Supplementary Section 8.

Electroluminescence measurements

Electroluminescence measurements were performed at 4 K in an Attocube Attodry 1000 system. A Keithley 2614B source-measure unit was used to simultaneously bias and measure the current through the device. The bias was applied to the top graphene contact while the bottom graphene and silicon back gate were grounded. Luminescence spectra were obtained using a Princeton instruments Acton SpectraPro SP-2500 spectrometer, with a 300 g mm^{-1} grating, alongside a PyLoN cryogenically cooled CCD camera.

Data availability

Images and source data that support the plots within this paper can be found at https://doi.org/10.48420/24306832. Source data are provided with this paper.

References

1. Geim, A. K. & Grigorieva, I. V. Van der Waals heterostructures. *Nature* **499**, 419–425 (2013).
2. Haigh, S. J. et al. Cross-sectional imaging of individual layers and buried interfaces of graphene-based heterostructures and superlattices. *Nat. Mater.* **11**, 764–767 (2012).
3. Frisenda, R. et al. Recent progress in the assembly of nanodevices and van der Waals heterostructures by deterministic placement of 2D materials. *Chem. Soc. Rev.* **47**, 53–68 (2018).
4. Yu, Q. et al. Graphene segregated on Ni surfaces and transferred to insulators. *Appl. Phys. Lett.* **93**, 113103 (2008).
5. Reina, A. et al. Transferring and identification of single- and few-layer graphene on arbitrary substrates. *J. Phys. Chem. C.* **112**, 17741–17744 (2008).
6. Dean, C. R. et al. Boron nitride substrates for high-quality graphene electronics. *Nat. Nanotechnol.* **5**, 722–726 (2010).
7. Reina, A. et al. Large area, few-layer graphene films on arbitrary substrates by chemical vapor deposition. *Nano Lett.* **9**, 30–35 (2009).
8. Wang, L. et al. One-dimensional electrical contact to a two-dimensional material. *Science* **342**, 614–617 (2013).
9. Castellanos-Gomez, A. et al. Deterministic transfer of two-dimensional materials by all-dry viscoelastic stamping. *2D Mater.* **1**, 011002 (2014).
10. Banszerus, L. et al. Ballistic transport exceeding 28 µm in CVD grown graphene. *Nano Lett.* **16**, 1387–1391 (2016).
11. Withers, F. et al. Light-emitting diodes by band-structure engineering in van der Waals heterostructures. *Nat. Mater.* **14**, 301–306 (2015).
12. Mayorov, A. S. et al. Micrometer-scale ballistic transport in encapsulated graphene at room temperature. *Nano Lett.* **11**, 2396–2399 (2011).
13. Cao, Y. et al. Quality heterostructures from two-dimensional crystals unstable in air by their assembly in inert atmosphere. *Nano Lett.* **15**, 4914–4921 (2015).
14. Rooney, A. P. et al. Observing imperfection in atomic interfaces for van der Waals heterostructures. *Nano Lett.* **17**, 5222–5228 (2017).
15. Long, G. et al. Achieving ultrahigh carrier mobility in two-dimensional hole gas of black phosphorus. *Nano Lett.* **16**, 7768–7773 (2016).
16. Pizzocchero, F. et al. The hot pick-up technique for batch assembly of van der Waals heterostructures. *Nat. Commun.* **7**, 11894 (2016).
17. Ghorbanfekr-Kalashami, H., Vasu, K. S., Nair, R. R., Peeters, F. M. & Neek-Amal, M. Dependence of the shape of graphene nanobubbles on trapped substance. *Nat. Commun.* **8**, 15844 (2017).
18. Rosenberger, M. R. et al. Nano-'squeegee' for the creation of clean 2D material interfaces. *ACS Appl. Mater. Interfaces* **10**, 10379–10387 (2018).
19. Purdie, D. G. et al. Cleaning interfaces in layered materials heterostructures. *Nat. Commun.* **9**, 5387 (2018).

20. Clark, N. et al. Scalable patterning of encapsulated black phosphorus. *Nano Lett.* **18**, 5373–5381 (2018).
21. Bandurin, D. A. et al. High electron mobility, quantum Hall effect and anomalous optical response in atomically thin InSe. *Nat. Nanotechnol.* **12**, 223–227 (2017).
22. Masubuchi, S. et al. Autonomous robotic searching and assembly of two-dimensional crystals to build van der Waals superlattices. *Nat. Commun.* **9**, 1413 (2018).
23. Mannix, A. J. et al. Robotic four-dimensional pixel assembly of van der Waals solids. *Nat. Nanotechnol.* **17**, 361–366 (2022).
24. Velický, M. et al. Mechanism of gold-assisted exfoliation of centimeter-sized transition-metal dichalcogenide monolayers. *ACS Nano* **12**, 12 (2018).
25. Desai, S. B. et al. Gold-mediated exfoliation of ultralarge optoelectronically-perfect monolayers. *Adv. Mater.* **28**, 4053–4058 (2016).
26. Longchamp, J.-N., Escher, C. & Fink, H.-W. Ultraclean freestanding graphene by platinum-metal catalysis. *J. Vac. Sci. Technol. B, Nanotechnol. Microelectron. Mater. Process. Meas. Phenom.* **31**, 020605 (2013).
27. Cheng, Z. et al. Toward intrinsic graphene surfaces: a systematic study on thermal annealing and wet-chemical treatment of SiO_2-supported graphene devices. *Nano Lett.* **11**, 767–771 (2011).
28. Ribeiro-Palau, R. et al. High-quality electrostatically defined Hall bars in monolayer graphene. *Nano Lett.* **19**, 2583–2587 (2019).
29. Kumaravadivel, P. et al. Strong magnetophonon oscillations in extra-large graphene. *Nat. Commun.* **10**, 3334 (2019).
30. Watanabe, K. & Taniguchi, T. Far-UV photoluminescence microscope for impurity domain in hexagonal-boron-nitride single crystals by high-pressure, high-temperature synthesis. *npj 2D Mater. Appl.* **3**, 40 (2019).
31. Zultak, J. et al. Ultra-thin van der Waals crystals as semiconductor quantum wells. *Nat. Commun.* **11**, 125 (2020).
32. Paur, M. et al. Electroluminescence from multi-particle exciton complexes in transition metal dichalcogenide semiconductors. *Nat. Commun.* **10**, 1709 (2019).
33. Cao, Y. et al. Enhancing and quantifying spatial homogeneity in monolayer WS_2. *Sci. Rep.* **11**, 14831 (2021).
34. Kim, H. H., Lee, S. K., Lee, S. G., Lee, E. & Cho, K. Wetting-assisted crack- and wrinkle-free transfer of wafer-scale graphene onto arbitrary substrates over a wide range of surface energies. *Adv. Funct. Mater.* **26**, 2070–2077 (2016).
35. Chan, J. et al. Reducing extrinsic performance-limiting factors in graphene grown by chemical vapor deposition. *ACS Nano* **6**, 3224–3229 (2012).
36. Jeong, H. J. et al. Improved transfer of chemical-vapor-deposited graphene through modification of intermolecular interactions and solubility of poly(methylmethacrylate) layers. *Carbon* **66**, 612–618 (2014).
37. Pálinkás, A. et al. The composition and structure of the ubiquitous hydrocarbon contamination on van der Waals materials. *Nat. Commun.* **13**, 6770 (2022).
38. Taychatanapat, T., Watanabe, K., Taniguchi, T. & Jarillo-Herrero, P. Electrically tunable transverse magnetic focusing in graphene. *Nat. Phys.* **9**, 225–229 (2013).
39. Son, S. K. et al. Graphene hot-electron light bulb: incandescence from hBN-encapsulated graphene in air. *2D Mater.* **5**, 011006 (2018).
40. Uri, A. et al. Mapping the twist-angle disorder and Landau levels in magic-angle graphene. *Nature* **581**, 47–52 (2020).
41. Cao, Y. et al. Unconventional superconductivity in magic-angle graphene superlattices. *Nature* **556**, 43–50 (2018).
42. Sharpe, A. L. et al. Emergent ferromagnetism near three-quarters filling in twisted bilayer graphene. *Science* **365**, 605–608 (2019).
43. Reale, F. et al. High-mobility and high-optical quality atomically thin WS_2. *Sci. Rep.* **7**, 14911 (2017).
44. Jain, A. et al. Minimizing residues and strain in 2D materials transferred from PDMS. *Nanotechnology* **29**, 265203 (2018).
45. Ren, K., Dai, W., Zhou, J., Su, J. & Wu, H. Whole-Teflon microfluidic chips. *Proc. Natl Acad. Sci. Usa.* **108**, 8162–8166 (2011).
46. Pizzocchero, F. et al. Chemical vapor-deposited graphene on ultraflat copper foils for van der Waals hetero-assembly. *ACS Omega* **7**, 22626–22632 (2022).
47. Kim, S. J. et al. Flat-surface-assisted and self-regulated oxidation resistance of Cu(111). *Nature* **603**, 434–438 (2022).
48. Chen, T. A. et al. Wafer-scale single-crystal hexagonal boron nitride monolayers on Cu (111). *Nature* **579**, 219–223 (2020).
49. Fukamachi, S. et al. Large-area synthesis and transfer of multilayer hexagonal boron nitride for enhanced graphene device arrays. *Nat. Electron.* **6**, 126–136 (2023).
50. Wang, M. et al. Single-crystal, large-area, fold-free monolayer graphene. *Nature* **596**, 519–524 (2021).
51. Li, J. et al. Wafer-scale single-crystal monolayer graphene grown on sapphire substrate. *Nat. Mater.* **21**, 740–747 (2022).
52. Masubuchi, S. et al. Deep-learning-based image segmentation integrated with optical microscopy for automatically searching for two-dimensional materials. *npj 2D Mater. Appl.* **4**, 3 (2020).
53. Kim, K. et al. Van der Waals heterostructures with high accuracy rotational alignment. *Nano Lett.* **16**, 1989–1995 (2016).
54. Scargle, J. D. Studies in astronomical time series analysis. II—Statistical aspects of spectral analysis of unevenly spaced data. *Astrophys. J.* **263**, 835 (1982).

Acknowledgements

We acknowledge support from the European Union's Horizon 2020 Research and Innovation programme: European Graphene Flagship Core3 Project (Grant Agreement No. 881603), European Quantum Flagship Project 2DSIPC (820378), European Research Council (ERC) Starter Grant EvoluTEM (Grant No. 715502 to S.J.H.), ERC Consolidator QTWIST (Grant No. 101001515 to R.G.), ERC Consolidator Grant 3DAddChip (Grant No. 819069 to C.M.), Marie Skłodowska-Curie fellowship PTMCnano (Grant No. 751883 to M.H.) and the Royal Society (R.G). In addition, we acknowledge support from the Engineering and Physical Sciences Research Council (EPSRC; Grant Nos. EP/V007033/1 and EP/V036343/1 to R.G.), the Graphene NOWNANO Centre for Doctoral Training (A.C., H.d.L., Y.G. and F.S.) and the China Scholarship Council (Grant Nos. 202106950021 to H.B, 201806280036 to W.W. and 201908890023 to Y.G.). This project was supported by the Henry Royce Institute for Advanced Materials, funded through EPSRC grants EP/R00661X/1, EP/S019367/1, EP/P025021/1 and EP/P025498/1. E. Tovari acknowledges support from OTKA Grant PD-134758 from the National Research, Development, and Innovation Office of the Ministry of Innovation and Technology of Hungary, and the Bolyai Fellowship of the Hungarian Academy of Sciences (Grant No. BO/00242/20/11).

Author contributions

R.G. and N.C. conceived the study. W.W., M.H., M.Z. and N.C. developed and tested the SiN_x membrane transfer. W.W. and N.C. developed the SiN_x transfer for the CVD-grown 2D material. A.C., E. Tovari, E.G.C., T.H.B. and A.S. translated the SiN_x transfer into UHV and fabricated experimental samples. S.S.-A., E. Tillotson and S.J.H. performed the electron microscopy characterization with help from W.W. Y.G., X.L., L.A.P. and A.V.K performed the electronic transport experiments and data analysis. J.H. performed the optical characterization. A.W., E.G.C. and H.d.L. performed the scanning probe micrroscopy and c-AFM measurements. F.S. applied the SiN_x transfer to patterned materials. H.B., C.M, P.V.W. and A.J.S supplied the CVD-grown transition-metal dichalcogenides. K.W. and T.T. supplied high-quality hBN crystals. R.G., N.C, W.W., M.H. and A.S. wrote the manuscript. All authors contributed

to the discussions and commented on the manuscript. W.W., N.C., M.H. and A.C. contributed to this work equally and can claim their leading role for job applications, interviews and talks.

Competing interests
The authors declare no competing interests.

Additional information
Extended data Extended data are available for this paper at https://doi.org/10.1038/s41928-023-01075-y.

Supplementary information The online version contains supplementary material available at https://doi.org/10.1038/s41928-023-01075-y.

Correspondence and requests for materials should be addressed to Nicholas Clark, Alex Summerfield or Roman Gorbachev.

Peer review information *Nature Electronics* thanks Lain-Jong Li and the other, anonymous, reviewer(s) for their contribution to the peer review of this work.

https://doi.org/10.1038/s41928-023-01075-y

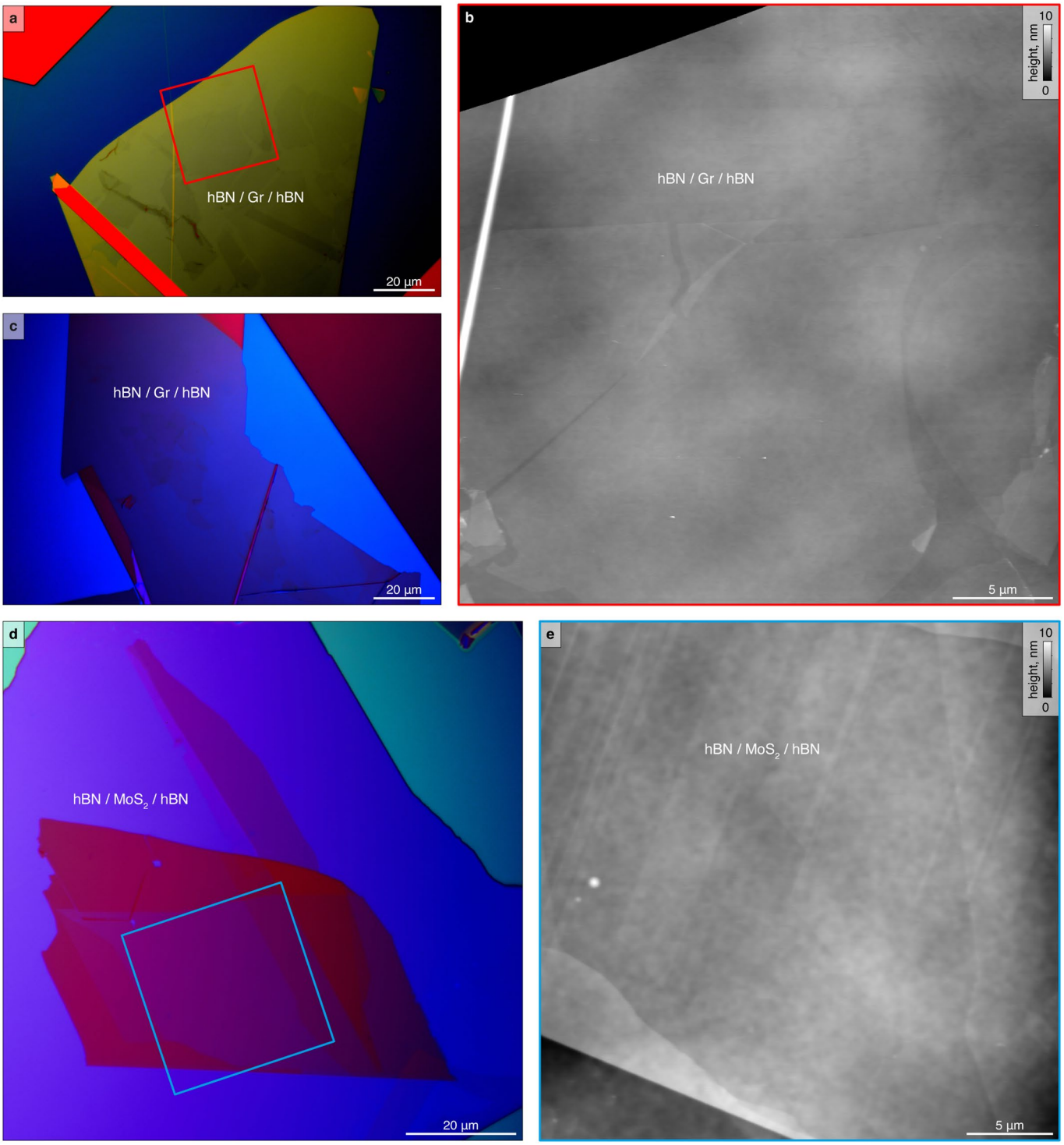

Extended Data Fig. 1 | Additional heterostructures. (**a**,**c**) Optical images of hBN/graphene/hBN stacks displaying complete absence of contamination bubbles between the layers, as confirmed by atomic force microscopy (AFM) topography scan (**b**) of area indicated in red box in (a). (**d**) MoS_2 crystal containing from 1 to 10 layer terraces encapsulated between two hBN crystals. (**e**) AFM topography scan of the area indicated by black box in (d). Heterostructures assembled using the following temperatures: top hBN pick up at 150°C, graphene pickup at 150°C or MoS_2 pickup at 40°C, drop off at 230°C for graphene and 290°C for MoS_2.

https://doi.org/10.1038/s41928-023-01075-y

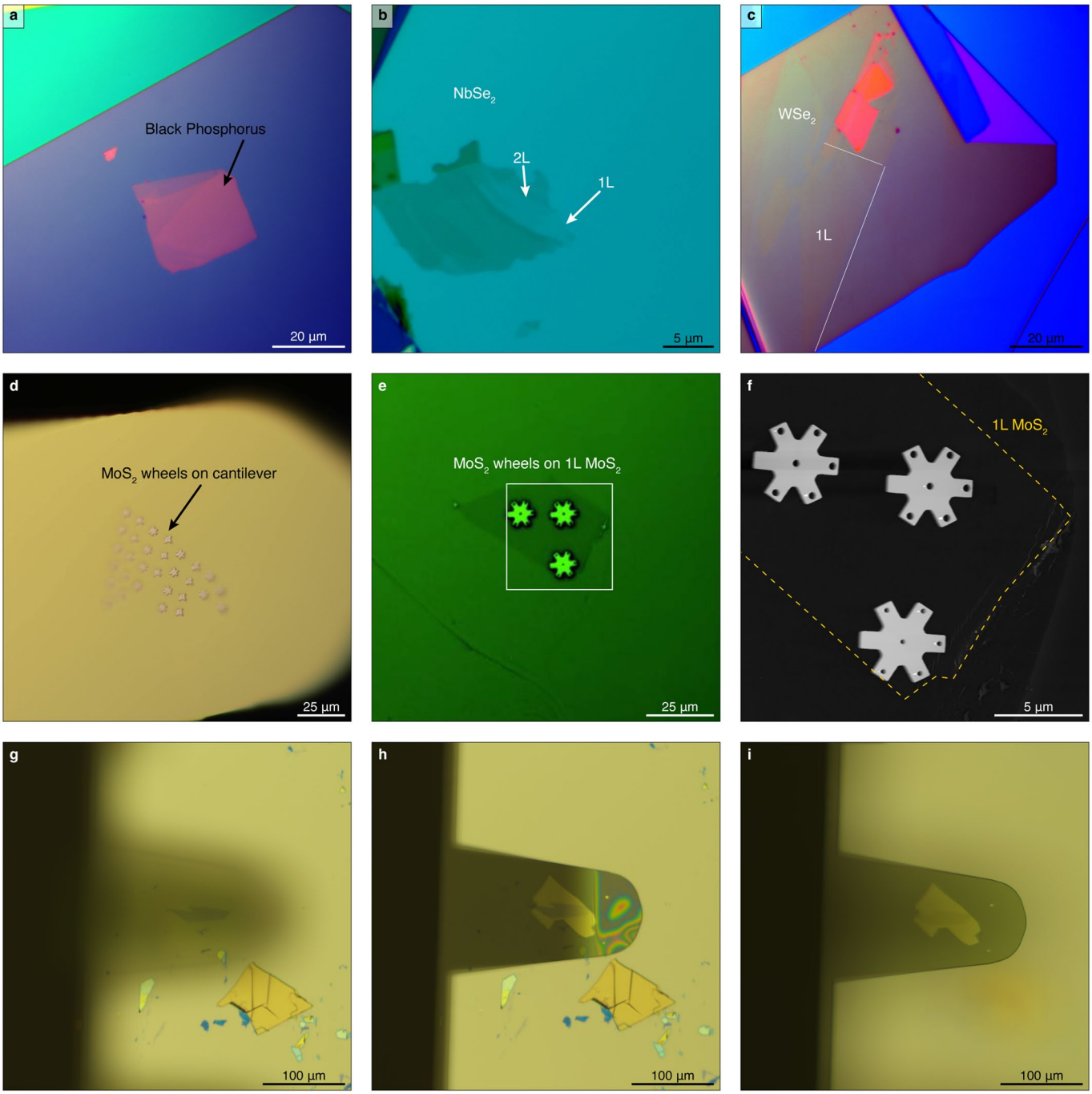

Extended Data Fig. 2 | Additional heterostructures, transfer of patterned 2D materials and immersed transfer in liquids. Optical micrographs of few-layer (**a**) black phosphorus, (**b**) niobium diselenide and (**c**) tungsten diselenide encapsulated in multilayer hBN crystals. All three materials have been picked up from an Si wafer spin-coated with polypropylene carbonate (PPC). (**d**) Multilayer MoS_2 wheel structures on an SiN_x cantilever afterpick-up from an Si/SiO_2 wafer at 150 °C. To prepare the wheels, MoS_2 was mechanically exfoliated onto Si/SiO_2 and suitable flakes (~40nm thick) were patterned with electron beam lithography, followed by CHF_3 etching. The wheels have been subsequently dropped off onto a monolayer MoS_2 crystal at 80 °C (**e**) and their topography mapped with AFM (**f**). Contrast of optical micrographs has been digitally enhanced to improve visibility. (**g-i**) Pick up of exfoliated graphene from SiO_2 surface in an acetone bath. (**g**) Alignment of cantilever over exfoliated graphene (**h**) contact of the cantilever carrying hBN crystal with the substrate (**i**) lift-off of the graphene away from the substrate.

https://doi.org/10.1038/s41928-023-01075-y

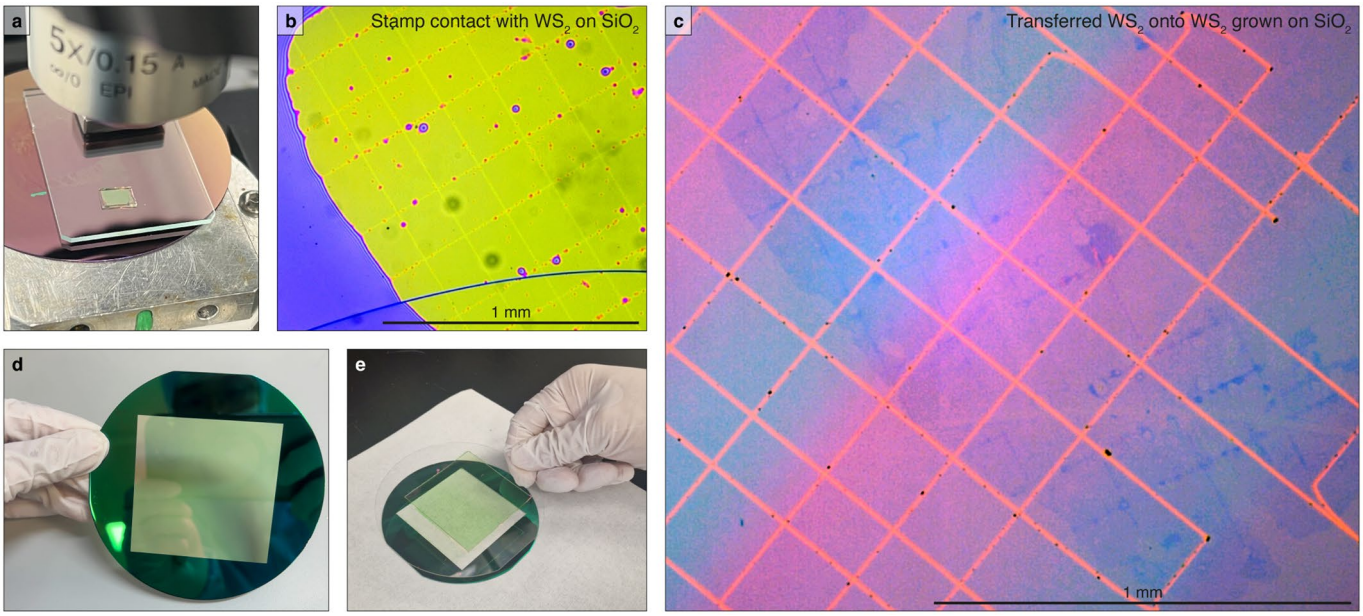

Extended Data Fig. 3 | Scalable laminate stamping transfer. (**a**) Pickup of TMD from growth substrate. Partial contact is clearly visible due to finite tilt angle between the two surfaces. (**b**) Metallized, PDMS supported SiN_x membrane during pickup of a WS_2 monolayer from its SiO_2 growth substrate. The contact area can be easily observed by the change in optical contrast. (**c**) The top layer of WS_2 from the region shown in panel (b) after transfer to few-layer WS_2 as grown on SiO_2. In both (b) and (c), Lines have been mechanically scratched into both surfaces, and the raw image contrast has been artificially enhanced to aid visualisation. Imperfections seen are due to differences in layer number, high points, and dust on both the original and target WS_2 layers. (**d**-**e**) Demonstration of 60 mm square SiN_x membrane (**d**) as fabricated and (**e**) after transfer to glass supported PDMS film for potential transfer of full 2" wafer scale CVD materials.